

# Preparation and characterisation of iron substituted $Mn_{1.7}Cu_{1.3-x}Fe_xO_4$ spinel oxides ( $x= 0, 0.1, 0.3, 0.5$ )

Justyna Ignaczak<sup>1\*</sup>, Yevgeniy Naumovich<sup>2</sup>, Karolina Górnicka<sup>3</sup>, Jan Jamroz<sup>4</sup>, Wojciech Wróbel<sup>4</sup>, Jakub Karczewski<sup>3</sup>, Ming Chen<sup>5</sup>, Piotr Jasiński<sup>1</sup>, Sebastian Molin<sup>1</sup>

<sup>1</sup> Faculty of Electronics, Telecommunications and Informatics, Gdańsk University of Technology,  
ul. G. Narutowicza 11/12, 80-233 Gdańsk, Poland

<sup>2</sup> Department of High Temperature Electrochemical Processes, Institute of Power Engineering,  
ul. Augustówka 36, 02-981 Warsaw, Poland

<sup>3</sup> Faculty of Applied Physics and Mathematics, Gdańsk University of Technology,  
ul. G. Narutowicza 11/12, 80-233 Gdańsk, Poland

<sup>4</sup> Faculty of Physics, Warsaw University of Technology, ul. Koszykowa 75, 00-662 Warsaw, Poland

<sup>5</sup> Department of Energy Conversion and Storage, Technical University of Denmark, Fysikvej, 2800 Kgs.  
Lyngby, Denmark

\*corresponding author: [justyna.ignaczak@pg.edu.pl](mailto:justyna.ignaczak@pg.edu.pl)

## Abstract

Spinel oxides with the general formula  $Mn_{1.7}Cu_{1.3-x}Fe_xO_4$  ( $x= 0, 0.1, 0.3, 0.5$ ) were prepared and evaluated in this work for their properties at high temperatures. The effect of partially substituting Cu by Fe has not been studied so far for this group of materials and is thus evaluated in this work.

$Mn_{1.7}Cu_{1.3-x}Fe_xO_4$  powders were synthesised by a soft chemistry process and studied in terms of crystallographic phase analysis, electrical conductivity, thermal expansion, and sinterability behaviour. The results show that the Fe content has a significant influence on the phase composition and the resulting properties. Characterisation of the dilatometry and conductivity coupled with XRD phase analysis across a wide temperature range allowed the relations between the materials properties and compositions to be observed. The results indicate that  $Mn_{1.7}Cu_{0.8}Fe_{0.5}O_4$  is a promising material for use as a protective coating for interconnects in intermediate temperature Solid Oxide Fuel Cells.

## 29 Introduction

30 Spinel oxides form a remarkable group of ceramic materials with a wide range of potential applications  
31 [1]. The general formula of a “regular” spinel is  $AB_2O_4$  with either a cubic or tetragonal structure, where  
32 A is a divalent cation, and B is a trivalent cation, which occupy tetrahedral and octahedral sites,  
33 respectively. The spinel mineral is  $MgAl_2O_4$ , which has a regular structure. A spinel can also adopt an  
34 “inverse” structure, where half of the trivalent B cations occupy the tetrahedral sites, and the divalent  
35 A cations and the remaining half of the B cations occupy the octahedral sites. Due to these broad  
36 possibilities, many different spinel materials can be synthesised. Indeed, spinels have found wide use  
37 in Li-ion batteries as electrodes [2], supercapacitor electrodes [3], thermal barrier coating material [4],  
38 as well as in other devices [5–7]. Depending on the chemical composition as well as on the preparation  
39 method/thermal history, spinels can be characterised by a broad range of electrical transport  
40 properties. It was reported that the electronic conductivity of a spinel occurs mainly by electron  
41 hopping between octahedral sites [8,9], and the cation arrangement can depend on the thermal  
42 history of the sample.

43 Manganese-copper-based spinels are interesting materials that have been studied for range of  
44 important applications [10–13]. The abundance and low toxicity of Mn and Cu makes the material of  
45 interest, especially as a possible replacement of Mn-Co-based spinels, where the mining issues and  
46 toxicity of cobalt are problematic. Mn-Cu spinels are already recognised as a potential catalyst for the  
47 steam reforming of methanol [14], as a ceramic film for spectrally selective solar-derived  
48 applications [15], and also as a protective coating on the interconnects in solid oxide fuel cells [16].

49 The phase diagram of Mn-Cu-O shows that a pure spinel phase forms only in a relatively narrow  
50 compositional and temperature window [17,18]. For this reason, most studied compositions have  
51 focused on  $Mn_2CuO_4$  or a slightly modified  $Mn_{1.7}Cu_{1.3}O_4$  [19–21]. A increased Cu content shifts the  
52 compositions towards a mixture of spinel and CuO, whereas a decreased Cu content, towards a mixture  
53 of manganese oxide and spinel.

54 Petric and Ling investigated the electrical conductivity of  $Mn_{1.7}Cu_{1.3}O_4$ , which achieved a very high value  
55 of 225 S/cm at 750 °C [22]. This is much higher than the electrical conductivity reported for the widely  
56 used  $MnCo_2O_4$  spinel ( $\sim 60 \text{ S cm}^{-1}$  at 800 °C). Since this work, interest in Mn-Cu spinels has increased.  
57 They have been tested as a protective coating for steel interconnects, and as a contacting mesh  
58 element in high temperature fuel cells [23–26].

59 Partial substitution of one of the cations is a well-known way to improve the properties of spinel-based  
60 ceramics. This approach has been extensively used to tailor the properties of  $MnCo_2O_4$  spinels. Partial

61 substitution of Co by either Fe or Cu has been reported to influence the electrical conductivity and  
62 thermal expansion [27–29]. Talic et al. showed that the addition of iron ( $\text{MnCo}_{1.5}\text{Fe}_{0.5}\text{O}_4$ ) decreased the  
63 electrical conductivity and the thermal expansion coefficient, whereas the addition of Cu  
64 ( $\text{MnCo}_{1.5}\text{Cu}_{0.5}\text{O}_4$ ) resulted in higher electrical conductivity and a higher thermal expansion  
65 coefficient [30]. Other studies considered the effect of the addition of Fe/Cu on high temperature  
66 corrosion and chromium evaporation of steel interconnects [31–34].

67 The effects of elemental substitutions in Mn-Cu-based spinels have been studied to a much lesser  
68 extent. Bhandage et al. have studied a  $\text{Cu}_x\text{Cd}_{1-x}\text{Mn}_2\text{O}_4$  system [11]. For  $x = 1$ , pure cubic phase spinel  
69 was obtained, whereas for a composition with  $x < 0.5$ , a tetragonal phase was found. The same author  
70 also studied the  $\text{Ni}_x\text{Cu}_{1-x}\text{Mn}_2\text{O}_4$  system [12]. Ni substitution in the Mn-Cu spinel was considered as a  
71 protective coating and for its effect on high-temperature corrosion protection by Joshi and Petric [35].  
72 Ni stabilised the cubic spinel phase and resulted in a small decrease of electrical conductivity.

73 A number of synthesis methods have been used for the preparation of different spinel powders,  
74 including modified sol-gel [36,37], EDTA gel [38], the glycine nitrate process [39], spray pyrolysis  
75 [28,30], co-precipitation [40], and solid state [41,42]. Among the reported methods, the sol-gel-derived  
76 routes seem to offer the advantage of cation mixing at the atomic level leading to high homogeneity  
77 and formation of small particle sizes [43].

78 In the present investigation, the  $\text{Mn}_{1.7}\text{Cu}_{1.3}\text{O}_4$  spinel was used as the starting material, and its  
79 derivatives with partial substitution of Cu by Fe were studied. The influence of iron substitution on its  
80 properties, related to SOFC interconnect protection, namely sintering behaviour, crystal structure, and  
81 electrical conductivity was evaluated.

82

## 83 **2. Experimental**

### 84 **2.1. Powder preparation**

85 Spinel powders with the general formula  $\text{Mn}_{1.7}\text{Cu}_{1.3-x}\text{Fe}_x\text{O}_4$ , where  $x=0, 0.1, 0.3, \text{ and } 0.5$ , were  
86 synthesised by a modified Pechini method [44]. Throughout the paper, the powders and sample  
87 compositions are abbreviated according to Table 1. The starting substrates used in the syntheses were  
88 hydrated nitrate salts of metals: manganese (II) nitrate ( $\text{Mn}(\text{NO}_3)_2 \cdot 4\text{H}_2\text{O}$ , Sigma Aldrich,  $\geq 97\%$ ), copper  
89 (II) nitrate ( $\text{Cu}(\text{NO}_3)_2 \cdot \text{H}_2\text{O}$ , Sigma Aldrich, 99.999%), and iron (III) nitrate ( $\text{Fe}(\text{NO}_3)_3 \cdot 9\text{H}_2\text{O}$ , Sigma Aldrich,  
90 99.999%). Water solutions of dissolved nitrates with known concentrations (pre-standardised  
91 thermogravimetrically) were mixed together in the proper molar ratio corresponding to the intended

92 nominal composition of the spinel powders. The water solutions containing all of the desired cations  
93 were heated under constant stirring to 80 °C (controlled using an insertion probe) on a magnetic  
94 stirring hot plate. Citric acid (C<sub>6</sub>H<sub>8</sub>O<sub>7</sub>, Sigma Aldrich, 99%), and EDTA ([CH<sub>2</sub>N(CH<sub>2</sub>CO<sub>2</sub>H)<sub>2</sub>]<sub>2</sub>, Sigma Aldrich,  
95 99%) were added to the solution under stirring as chelating agents in the molar ratio 2:1:1-TMI (total  
96 molar ions). To control the pH at the desired level of 8, diluted ammonia (25% aqueous solution) was  
97 added dropwise. To start the transesterification process, ethylene glycol (C<sub>2</sub>H<sub>6</sub>O<sub>2</sub>, Sigma Aldrich, 98%)  
98 was added under continuous stirring, in the amount to obtain a ratio of 1 mol of polyalcohol to 1 mol  
99 of metal cations. The liquid precursor was then held at 80 °C until a dense gel-like structure was  
100 obtained. It was further dried at 130 °C for 4 h. The resulting material was placed in a muffle furnace  
101 and heated to 400 °C for 2 h. The obtained powder was ground in an agate mortar and further calcined  
102 at 900 °C for 2 h. In the end, the powders were again ground in the agate mortar and used for further  
103 studies.

104

## 105 **2.2. Pellet preparation**

106 Ceramic pellets were prepared from the synthesised powders by uniaxial pressing in a hydraulic press  
107 (Carver, USA). The powders were compacted using 54 MPa pressure. The obtained disk-shaped green  
108 bodies had a diameter of ~16 mm and a thickness of 1.5–2 mm. The pressed pellets were sintered at  
109 three different temperatures: 900 °C, 1000 °C, and 1100 °C in air. Heating and cooling rates of  
110 3.6 °C min<sup>-1</sup> were used with a dwell time of 2 h. The dimensions of the sintered pellets were measured  
111 (using a Mitutoyo micro-caliper) to calculate the linear shrinkage. The porosity of the sintered pellets  
112 was determined from analyses of SEM images of polished cross-sections. For each sample, ten images  
113 were taken at the same magnification, and these images were analysed using the ImageJ software [44].

114

## 115 **2.3. Materials characterisation**

116 The x-ray diffraction (XRD) technique was used to determine the phase composition and the crystal  
117 structure of the fabricated powders. The measurements of the synthesised powders were conducted  
118 at room temperature using a Bruker D2 Phaser 2<sup>nd</sup> generation diffractometer with CuKα radiation  
119 (λ = 1.5404 Å) and XE-T detectors. Data were collected from 2θ = 10° to 90° with a step size of 0.01°  
120 and accounting time of 0.2 sec for each step. The results were processed by means of LeBail refinement  
121 using the Bruker Topas software.

122 High temperature X-ray powder diffraction data were collected on a Philips X'Pert Pro diffractometer,  
123 fitted with an X'Celerator detector, using Ni filtered Cu-Kα radiation (I<sub>1</sub> = 1.54056 Å and I<sub>2</sub> = 1.54439 Å).  
124 Elevated temperature measurements were performed using an Anton-Paar HTK 1200 high

125 temperature camera. Data were collected in flat plate  $\theta/\theta$  geometry on a Pt-coated sample holder.  
126 Calibration was carried out with an external  $\text{LaB}_6$  standard. Diffraction patterns were acquired at room  
127 temperature and at 50 °C intervals from 50 °C to 850 °C in air. Data at room temperature and at 850 °C  
128 were collected over the range 5–105°  $2\theta$ , in steps of 0.033°, with an effective scan time of 120 s per  
129 step. Shorter scans were performed for intermediate temperatures with an effective scan time of 40 s  
130 per step.

131 Thermogravimetric analysis (TGA) of the studied oxides was performed using a Netzsch TG 209 F3  
132 Tarsus thermobalance. The measurements were carried out both in air and argon atmospheres. The  
133 mass change was observed up to 900 °C with a heating and cooling rate of 3 °C  $\text{min}^{-1}$ .

134 Dilatometric studies of the sintering and thermal expansion were carried out using a Netzsch DIL402  
135 dilatometer. Measurements were performed in a synthetic air atmosphere with a heating rate of 5 °C  
136  $\text{min}^{-1}$ , with a 15 minutes isothermal step at 1100 °C and a cooling rate of 3 °C  $\text{min}^{-1}$ .

137 The phase diagram of Cu-O<sub>2</sub> was calculated using the FACTSAGE software and databases [45].

138 Scanning electron microscopy (SEM) investigation of the powders and pellet cross sections were  
139 carried out on a Phenom XL (Thermo Fisher Scientific) desktop SEM equipped with an integrated  
140 energy dispersive X-ray (EDX) microanalyser. For preparation of the pellet cross sections, samples were  
141 mounted in epoxy (EpoFix, Struers) and then polished on a semi-automatic Struers Tergamin-20  
142 machine down to a 1  $\mu\text{m}$  finish.

143 The electrical conductivity of the pellets was estimated by employing the van der Pauw method [46].  
144 The samples were heated to 900 °C and measured down to 200 °C with decrements of 50 °C in air. The  
145 activation energy,  $E_a$ , was calculated using the formula, derived from the Arrhenius equation:

146 
$$\ln\sigma T = \frac{-E_a}{k} \times \frac{1}{T} + \ln\sigma_0, \quad (\text{Eq.1})$$

147 where  $\sigma$  — electrical conductivity,  $T$  — temperature,  $\sigma_0$ — pre-exponential factor,  $E_a$ — activation  
148 energy, and  $k$  — Boltzmann's constant.

149 Electrical conductivity data were corrected for sample porosity with using the Brueggemann  
150 asymmetric model, according to the following formula [47]:

151 
$$\sigma = \sigma_m \cdot \frac{1}{(1-p)^{\frac{3}{2}}}$$

152 Where  $\sigma$  is the corrected conductivity,  $\sigma_m$  is the measurement conductivity and  $p$  is sample porosity.

153

154

155

### 156 3. Results and discussion

#### 157 3.1. Chemical, microstructural and sintering characterisation of the powders

##### 158 Chemical and morphological analysis of the powders

159 After the milling process, the powders were characterised for their elemental compositions,  
 160 morphologies, and phase structures. EDX analyses were performed on the powders to determine the  
 161 atomic compositions of the calcined powders. The results of the analyses are presented in Table 1  
 162 (with the accuracy of EDX method +/- 1%). The calculated Mn/(Mn+Fe) and Fe/(Fe+Cu) cation ratios  
 163 correspond well to the expected stoichiometries.

164

165 **Table 1.** Chemical composition of powders determined by means of EDX and sample's names used in  
 166 this paper.

Desired composition	Sample name	Metal ratio			Mn / Cu+Fe	Fe / Fe+Cu	Corresponding spinel composition
		Mn	Cu	Fe			
$\text{Mn}_{1.7}\text{Cu}_{1.3}\text{O}_4$	0Fe	0.56	0.44	-	1.27	-	$\text{Mn}_{1.68}\text{Cu}_{1.32}\text{O}_4$
$\text{Mn}_{1.7}\text{Cu}_{1.2}\text{Fe}_{0.1}\text{O}_4$	01Fe	0.59	0.38	0.03	1.43	0.07	$\text{Mn}_{1.73}\text{Cu}_{1.15}\text{Fe}_{0.12}\text{O}_4$
$\text{Mn}_{1.7}\text{Cu}_1\text{Fe}_{0.3}\text{O}_4$	03Fe	0.56	0.34	0.10	1.27	0.23	$\text{Mn}_{1.69}\text{Cu}_{0.99}\text{Fe}_{0.32}\text{O}_4$
$\text{Mn}_{1.7}\text{Cu}_{0.8}\text{Fe}_{0.5}\text{O}_4$	05Fe	0.57	0.25	0.18	1.32	0.42	$\text{Mn}_{1.69}\text{Cu}_{0.76}\text{Fe}_{0.54}\text{O}_4$

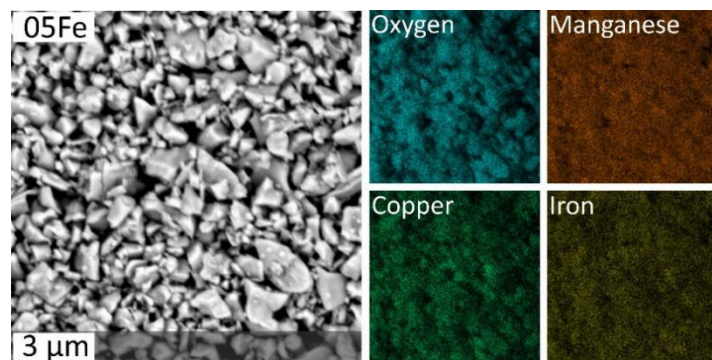
167

168 Figure 1 presents a representative SEM micrograph of the 05Fe powder after calcination at 900 °C and  
 169 after milling in an agate mortar. All of the powders were composed of micron-sized particles (~1–3 μm)  
 170 without the presence of larger agglomerates. No influence of iron substitution on the particle size  
 171 could be observed.

172

173





174

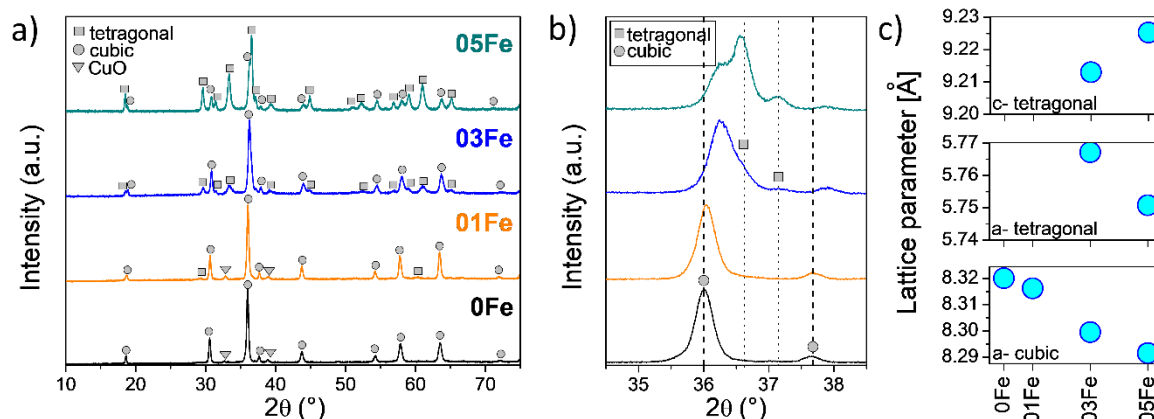
175 **Figure 1.** Scanning electron microscopy image and energy dispersive elemental analysis of the 05Fe  
 176  $(\text{Mn}_{1.7}\text{Cu}_{0.8}\text{Fe}_{0.5}\text{O}_4)$  powder.

177 **Room-temperature XRD analysis of the powders**

178 The room temperature XRD patterns of the calcined powders are shown in Figure 2a (full measured  
 179 range) and 2b (enlargement of the main peak region). The non-substituted 0Fe powder revealed the  
 180 existence of a cubic spinel phase (space group  $Fd\text{-}3m$ , ICDD card #35-1030) with a possible very small  
 181 addition of CuO (estimated to <3 vol.%, monoclinic structure, space group  $c2/c$ , #45-937). The  
 182 observation of these two phases is in agreement with the Cu-Mn-O phase diagram, where single-phase  
 183 cubic might decompose at low temperatures to spinel +  $\text{MnO}_2$ , or to  $\text{MnO}_2 + \text{CuO}$  [17,18,20]. A quite  
 184 similar structure was observed for the 01Fe powder. Only the cubic spinel and a small amount of  
 185 another phase could be seen. It must be noted that the peaks ascribed to CuO might also have been  
 186 caused by the cubic (#35-1030) or tetragonal ( $\text{CuMn}_2\text{O}_4$ , #71-1141) spinel phase. Due to overlapping  
 187 peaks and small relative intensity, the exact determination of the minority phase is not possible. The  
 188 presence of minor phase impurities in  $\text{Cu}_{1.3}\text{Mn}_{1.7}\text{O}_4$  is known in the literature, for example, Bobruk  
 189 et al. observed the same level of CuO-attributed peaks in this material, synthesised by EDTA-gel  
 190 processes and calcined at 700 °C [38]. The introduction of iron shifted the  $\sim 36^\circ$  peak position towards  
 191 the higher  $2\theta$  angle, evidencing contraction of the unit cell, compliant with a smaller size of the Fe  
 192 cations than Cu cations.

193 The increase in Fe-content resulted in the formation of a new phase, which can be attributed to a  
 194 tetragonal spinel structure (space group:  $I41/amd:2$ ) [48]. No indications of iron oxides could be found  
 195 in the spectra either. For the 03Fe powder, the cubic spinel peak had the highest intensity, whereas  
 196 for the 05Fe powder, the tetragonal phase dominated.





197

198 **Figure 2.** X-ray diffraction patterns of powders synthesised via the EDTA-CA gel process after  
 199 calcination at 900 °C (a, b). Lattice parameters (at room temperature), determined by structure  
 200 fitting of XRD patterns for spinel powders calcined at 900 °C (c).

201

202 The lattice parameters determined by structure fitting of the cubic Fd-3m space group and tetragonal  
 203 I41/amd:2 are plotted in Figure 2c and summarised in Table 2. The cubic spinel phase changed the unit  
 204 cell size (“a” parameter) linearly with the substitution of copper with iron. For the tetragonal phase,  
 205 the unit cell size showed a more complex behaviour. The “a” parameter decreased its value, whereas  
 206 the “c” parameter increased.

207 The formation of the tetragonal phase in the Mn-Cu spinel can be explained by the Jahn-Teller effect,  
 208 i.e. the elongation of the octahedral in the “c” direction [49]. This was caused by the presence of  
 209 octahedrally coordinated Mn<sup>3+</sup> cations (or possibly also Cu<sup>2+</sup>) [49,50]. Mn-Cu spinels are interesting as  
 210 materials which contain two Jahn-Teller ions: Mn<sup>3+</sup> and Cu<sup>2+</sup> [18]. Baffier and Huber argued that for the  
 211 formation of a tetragonal structure, the relative concentration of Mn<sup>3+</sup> ions needs to be high, i.e. >50%  
 212 of the sites [10,51]. The addition of iron thus resulted in the formation of Mn<sup>3+</sup> in octahedral positions  
 213 (or Cu<sup>2+</sup>), which allowed for the incorporation of the copper cations into the spinel structure. The  
 214 elongation of the unit cell in one direction (“c”) was followed by contraction of the unit cell in the “a”  
 215 direction.

216 The effect of cation substitution in the spinel structure cannot be resolved simply due to the complexity  
 217 of the structure, i.e. the presence of tetrahedral and octahedral positions and multiple possible valence  
 218 states of the cations. Due to the multitude of the possible arrangements and cation sizes, it is hard to  
 219 determine where the newly introduced cations are situated. As evidenced by XRD, partial substitution  
 220 of Cu by Fe led to the decrease of the lattice parameter “a”, as shown in Table 2. In general, iron cations



221 are smaller than copper cations, so a decrease of the cell-size parameter can be expected. Manganese  
 222 has a strong tendency to occupy the octahedral position. Due to the high Cu content in the  $Mn_{1.7}Cu_{1.3}O_4$   
 223 spinel, some Cu should also occupy the octahedral position, with the remaining Cu in the tetrahedral  
 224 position. The situation is also complicated by the fact that, at room temperature, the compositions rich  
 225 in iron (03Fe and 05Fe) are not single phase — they form a mixed cubic-tetragonal oxide, where the  
 226 cations' distributions will be further confounded. Therefore, in this paper, we do not propose any  
 227 specific cationic distribution, as it is far too complex and uncertain in our view. A summary of the  
 228 reported possible cation distributions in the Mn-Cu spinels can be found in [18].

229

230 **Table 2.** Lattice parameters for cubic and tetragonal phases determined by Le Bail refinement (at  
 231 room temperature).

Powder	Phase:	Cubic	Tetragonal			
		$a_c$ [Å]	$a_T$ [Å]	$a_T'$ [Å]	$c_T$ [Å]	$c_T / a_T'$
0Fe	C	8.3201(5)				
01Fe	C	8.3162(1)				
03Fe	C+T	8.2995(4)	5.7672(2)	8.13175	9.2133(2)	1.13
05Fe	C+T	8.2915(6)	5.7508(3)	8.1086	9.2253(4)	1.14

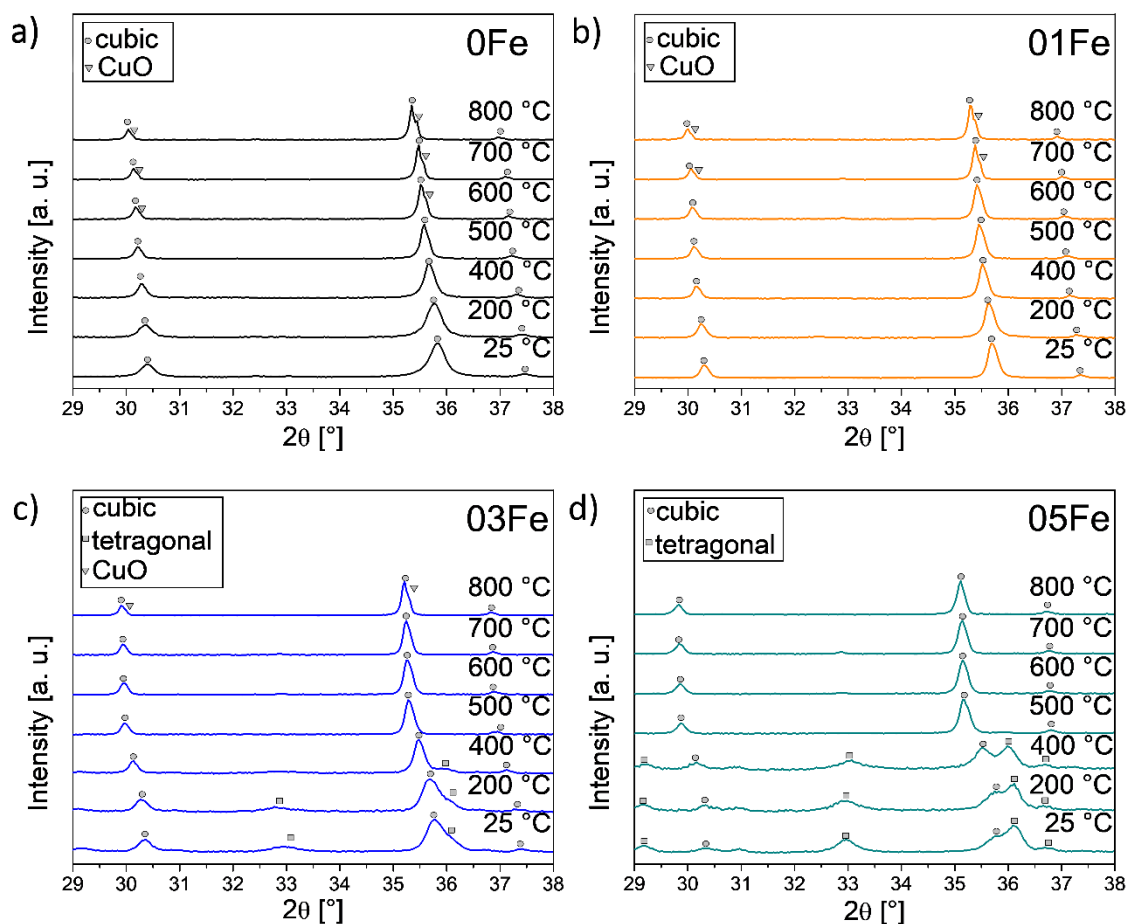
232

### 233 High-temperature XRD analysis of the powders

234 In order to follow the development of the phase-composition of the materials vs. temperature, in-situ  
 235 high-temperature XRD analyses were performed. The results are presented in Figure 3a–d.

236 For the 0Fe and 01Fe, the cubic phase did not change upon heating. Above 500 °C, the occurrence of  
 237 a new phase could be noticed for both powders. It is ascribed to CuO, which is in line with the phase  
 238 diagram [17] and discussion by Martin and Petric [20]. According to the phase diagram, the pure spinel  
 239 phase was stable in only a quite narrow temperature window (roughly between 500 °C and 600 °C).  
 240 For the 03Fe and 05Fe powders, where the cubic and tetragonal phases co-existed at room  
 241 temperature, transformation into a single cubic phase was observed at >400 °C. In the case of the 05Fe  
 242 powder, the tetragonal phase remained stable at 400 °C, whereas for the 03Fe powder, it seemed to  
 243 disappear at 400 °C. CuO also seemed to form in the 03Fe powder, whereas it was not detected in the  
 244 05Fe powder. The addition of Fe stabilised the spinel phase, which was a mixture of tetragonal-cubic  
 245 below 500 °C and transformed into a fully cubic spinel at >500 °C.



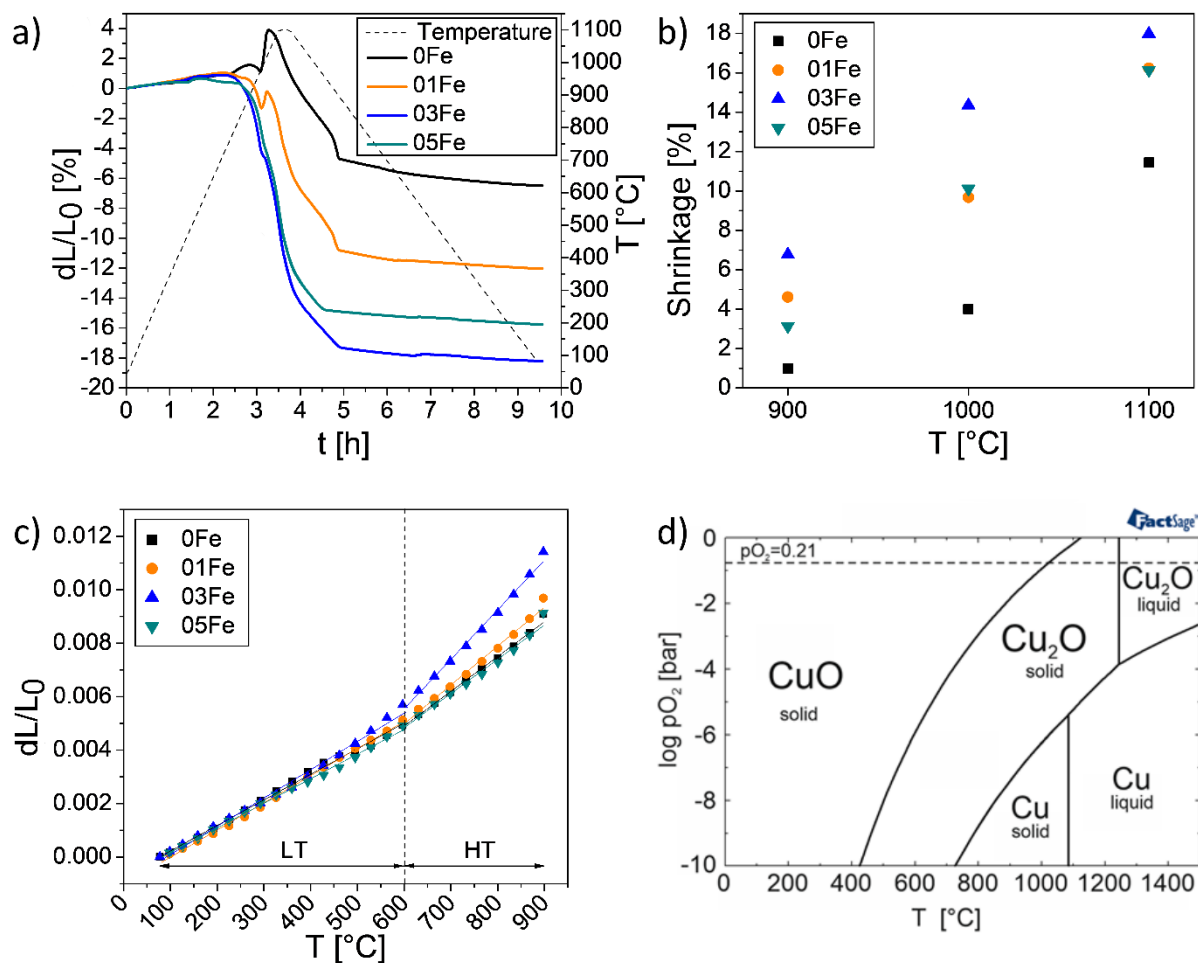


246

247 **Figure 3.** High-temperature XRD (25–800 °C in air) patterns for the powders: 0Fe(a), 01Fe (b), 03Fe  
 248 (c), and 05Fe (d).

249 **Dilatometry study**

250 Following the phase characterisation was the determination of the sintering properties of the prepared  
 251 compounds. A dilatometry study was performed in order to determine the shrinkage profiles of the  
 252 compacted powders (up to 1100 °C) and thermal expansion coefficient (TEC) values. In addition to the  
 253 measurements performed in the dilatometer, the diameters of the pellets were analysed before and  
 254 after ex-situ sintering in a furnace at different temperatures (900 °C, 1000 °C, and 1100 °C). The  
 255 dilatometry curves and values of relative shrinkage for the pellets are presented in Figure 4a–c.



256

257 **Figure 4.** Dilatometry results (in air) for sintering of the powders (a), relative shrinkage of the pellets  
 258 measured after sintering the green bodies at 900 °C, 1000 °C, 1100 °C (b), thermal expansion of the  
 259 spinel pellets, pre-sintered at 1100°C (cooling cycle from 900 °C in air) (c), and phase diagram of Cu-  
 260 O<sub>2</sub> showing the phase change of CuO to Cu<sub>2</sub>O (d).

261

262 The sintering behaviour of the materials differed considerably (Figure 4a). Intense expansion was  
 263 visible, especially for the non-iron-doped spinel, upon heating at ~1000 °C. The sample expanded by  
 264 ~4% within a few minutes, and then the sintering began. Quite similar behaviour was visible for the  
 265 01Fe powder, but to a smaller extent, potentially due to the earlier onset of sintering, as the sample  
 266 started to sinter at ~850–900 °C. The observed behaviour can be attributed to reduction of the CuO  
 267 phase, which formed upon heating of the spinel, as described in the HT-XRD discussion (see Figure 3).  
 268 CuO phase reduced into the Cu<sub>2</sub>O phase in this temperature range (~1000 °C), well in line with the Cu-  
 269 O-temp phase diagram presented in Figure 4d and the literature [52,53]. For the 03Fe and 05Fe  
 270 materials, where less or no CuO was detected in the XRD spectra, no such peaks in the dilatometry

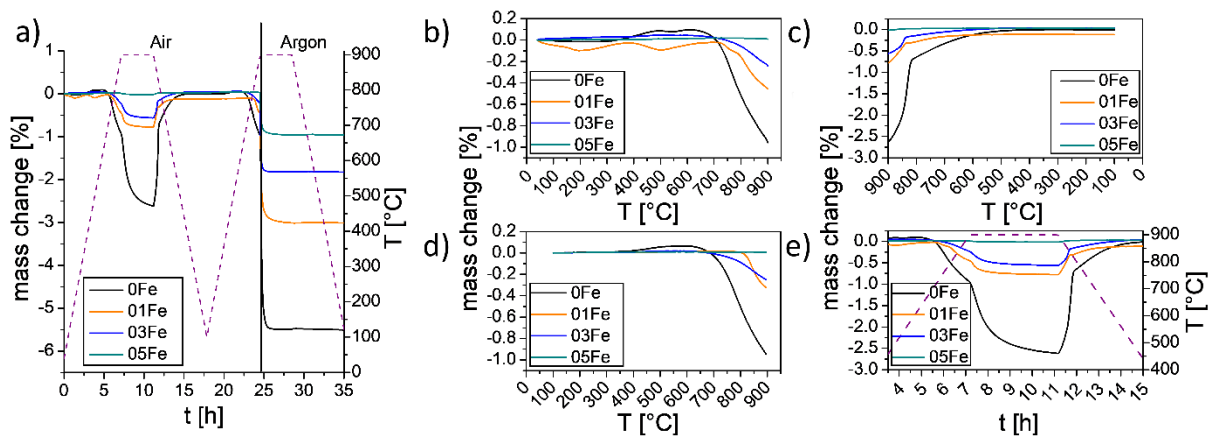
271 curves were visible. These powders started to sinter at  $\sim 800$  °C and followed a regular sintering  
272 pattern. The largest shrinkage was observed for the 03Fe sample ( $\sim 18\%$ ), followed by the 05Fe sample  
273 ( $\sim 16\%$ ). The continuous dilatometry results were confirmed by the ex-situ pellet diameter  
274 measurements: the smallest shrinkage was obtained for the 0Fe samples, followed by 01Fe and 05Fe,  
275 while the largest shrinkage was obtained for the 03Fe sample. The shrinkage values (Figure 4 b)  
276 demonstrate that iron doping sufficiently enhanced the sinterability of the studied materials, however  
277 fabrication of the ceramics with low porosity in air required temperatures above 1000 °C.

278 Thermal expansion coefficients were determined using data collected during cooling of the samples  
279 from 900 °C (samples were sintered in air at 1100 °C). As the curves were not linear in the 50–900 °C  
280 temperature range, the analysis region was divided into high temperature (600–900 °C) and low  
281 temperature (50–600 °C) intervals. The calculated TEC values are presented in Table 5. For the high  
282 temperature domain, thermal expansion demonstrated a complex effect of the iron doping, with an  
283 apparent maxima for the 03Fe ceramic. In the low temperature region, all of the sintered samples had  
284 a TEC of  $9.2\text{--}10.6 \times 10^{-6} \text{ K}^{-1}$ . In general, iron substitution did not have a strong influence on the thermal  
285 expansion.

#### 286 **Thermogravimetric analysis**

287 In addition to dilatometry, thermogravimetric analyses were performed. TGA revealed that  $\text{Mn}_{1.7}\text{Cu}_{1.3-}$   
288  $\text{xFe}_x\text{O}_4$  complex oxides demonstrated sufficient activity in oxygen exchange with the environment  
289 (Figure 5a–e). For the 0Fe, upon heating from room temperature to 900 °C, the sample initially gained  
290 weight ( $\sim 0.05\%$ ), which started at  $\sim 400$  °C, then at around 700 °C it started losing weight (Figure 5b  
291 first cycle of heating, and Figure 5d second cycle of heating). The sample with no iron was the only one  
292 to show no notable weight increase upon heating. The addition of iron suppressed the weight loss  
293 effect. For the 01Fe and 03Fe, the weight loss started at  $\sim 700$  °C and had a much smaller extent than  
294 the weight loss of the 0Fe. For the 0Fe powder, at isothermal hold at 900 °C, the weight change had  
295 not stabilised after 2 hours, which indicates relatively slow equilibration. The 01Fe and 03Fe powders  
296 seemed to stabilise their weight change faster (Figure 5e). For the 05Fe sample, neither weight gain  
297 nor weight loss was found. The 05Fe powder was practically inert in air, which supports the expectation  
298 of good stability in oxidising atmospheres at high temperatures. When cooling (Figure 5d), the mass  
299 change process was reversible, which confirms that this phenomenon is related to the stability of the  
300 tested materials and the oxidising atmosphere. The weight loss can be explained as a result of the  
301 formation of a CuO phase: the O/Cu ratio was lower in the CuO than in the spinel, therefore  
302 segregation of the CuO resulted in net loss of weight. At high temperature ( $\sim 900$  °C) the reduction of  
303 CuO to  $\text{Cu}_2\text{O}$  is also possible, visible in Figures 5c and 5e, in-line with the phase diagram presented in

304 Figure 4d. The weight loss trend corresponds well with the amount of possible CuO formation: for the  
 305 05Fe, where no CuO was detected upon heating, there was no weight loss, and the sample was stable  
 306 upon heating, while for the 0Fe, it was very prominent. One can note that the behaviour of the 03Fe  
 307 demands presence of traces of CuO, confirming the XRD observation. This might explain the behaviour  
 308 of the dilatometric curve for this material as well as its electric conductivity: the amount of iron in the  
 309 03Fe was not sufficient to keep the Cu in the cubic phase, so CuO particles grew during heating, which  
 310 led to the rise of the TEC and changes in electrical conductivity.



311  
 312  
 313 **Figure 5.** Mass change of the Mn<sub>1.7</sub>Cu<sub>1.3-x</sub>Fe<sub>x</sub>O<sub>4</sub> powders in air as a function of time (a), first heating  
 314 ramp (b), first cooling ramp (c), second heating ramp (d), and isothermal hold after first heating ramp  
 315 (e).

### 316 3.2. Electrical conductivity characterisation of the spinels

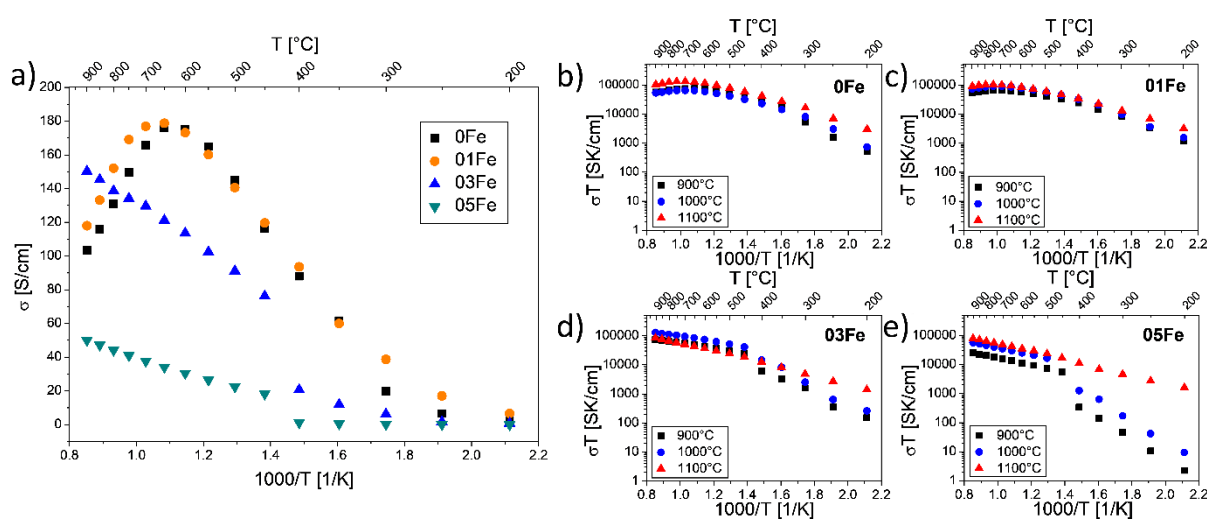
317 The electrical properties of the materials were analysed by studying the DC electrical transport  
 318 properties of the sintered pellets in air in the temperature range 900–200 °C. To evaluate the effects  
 319 of porosity and thermal treatment in general, pellets prepared from the 0Fe, 01Fe, 03Fe and 05Fe  
 320 powders were sintered at either 900 °C, 1000 °C, or 1100 °C in air. The results of the measurements  
 321 are presented in Figure 6a–e.

322 The behaviour of the samples depended on the iron substitution level, as summarised in Figure  
 323 6a. For the sample without iron (0Fe, Figure 6b) and with low iron content (01Fe, Figure 6c), the  
 324 electrical behaviour was notably different than for the samples with higher iron content (03Fe and  
 325 05Fe, Figures 6d and 6e, respectively). For the 0Fe and 01Fe, the maximum electrical conductivity was  
 326 reached at ~650 °C. The maximum conductivity value was quite similar, reaching ~180 S cm<sup>-1</sup>, which  
 327 can be considered very high (the small difference between the samples is within the experimental  
 328 error margin of ±5%). Below the maximum, the conductivity was thermally activated, whereas above  
 329 the maximum, the conductivity decreased with temperature increase. The point (temperature) of

330 conductivity maximum coincided with the point where the spinels started losing weight. This was thus  
 331 also connected to the formation of the CuO phase. Similar effects have been described by Martin and  
 332 Petric [20]. They also measured thermopower and determined that the majority of carriers are  
 333 electron holes (p-type conductivity).

334 For the samples with higher iron content, i.e. the 03Fe and 05Fe, the conductivity exhibited a clear  
 335 transition point, where the levels of electrical conductivity step-changed, and for which different  
 336 activation energies were found. The transition temperature was  $\sim 400$  °C and was caused by a phase  
 337 transition from mixed cubic-tetragonal phases to a pure cubic spinel phase (at high temperatures).  
 338 Interestingly, the 03Fe and 05Fe pellets sintered at 1100 °C did not show such a phase transition; only  
 339 a slight change of slope of the conductivity curve.

340 Samples with higher iron content showed generally lower conductivity values and a regular thermally  
 341 activated behaviour across the full temperature range. For the 03Fe sample, the conductivity was  
 342 highest after sintering at 1000 °C; sintering at a higher temperature reduced the conductivity. All of  
 343 the other compositions showed an increase of electrical conductivity upon increasing the sintering  
 344 temperature. The 03Fe sample showed a conductivity value of  $\sim 120$  S  $\text{cm}^{-1}$ , whereas the 05Fe sample  
 345 had a conductivity of  $\sim 30$  S  $\text{cm}^{-1}$  at 650 °C. As shown in Figure 6, due to the thermal activation across  
 346 the full temperature range, the electrical conductivity of the 03Fe sample became highest for  
 347 temperatures above 800 °C. Although the electrical conductivity values clearly depended on the iron  
 348 content, they can all be considered relatively high. Based on the results, it can be stated that the  
 349 electrical conductivity of the tetragonal phase (the low temperature phase) is greatly reduced in  
 350 comparison to the conductivity of the cubic phase.



351  
 352 **Figure 6.** Electrical conductivity plot of the 0Fe, 01Fe, 03Fe and 05Fe samples measured on pellets  
 353 sintered at 900 °C (a)- results were corrected for sample porosity. Arrhenius plots of electrical

354 conductivity as a function of pellet sintering temperatures (900 °C / 1000 °C / 1100 °C). Results were  
 355 not corrected for sample porosity.

356 Based on the Arrhenius plots (Figure 6b–e), the activation energies of the electrical  
 357 conductivity were calculated and are presented in Table 3. Due to the visible change in the slopes, the  
 358 activation energies were calculated separately for two temperature ranges: 450–650 °C and 200–  
 359 400 °C. These two ranges have distinctly different value levels. At high temperatures, the activation  
 360 energies were rather low, with values in the range 0.20–0.30 eV and did not seem to depend on the  
 361 sintering temperature. At lower temperatures, variation of the activation energies was quite  
 362 significant. The lowest values were found for the highest sintering temperature of 1100 °C (between  
 363 0.26 eV for the 05Fe sample, and 0.37 eV for the 0Fe) and were only slightly higher than the values  
 364 obtained at high temperatures. For lower sintering temperatures, the activation energies were in the  
 365 range of 0.4 to 0.7 eV. In general, the obtained values are in agreement with typical reported values  
 366 for different spinels [29,30,38]. The difference between the low and high temperature values of the  
 367 activation energy may be connected to different grain and grain boundary contributions to the total  
 368 electrical conductivity [54].

369

370

371 **Table 3.** Thermal expansion coefficients of the sintered spinels (from Figure 4c) and activation energy  
 372 of the electrical conductivity ( $E_A$ ) fitted according to Eq. 1 for two temperature ranges (200–400 °C  
 373 and 450–650 °C) for each featured material sintered at three temperatures (from Figure 6b–e).

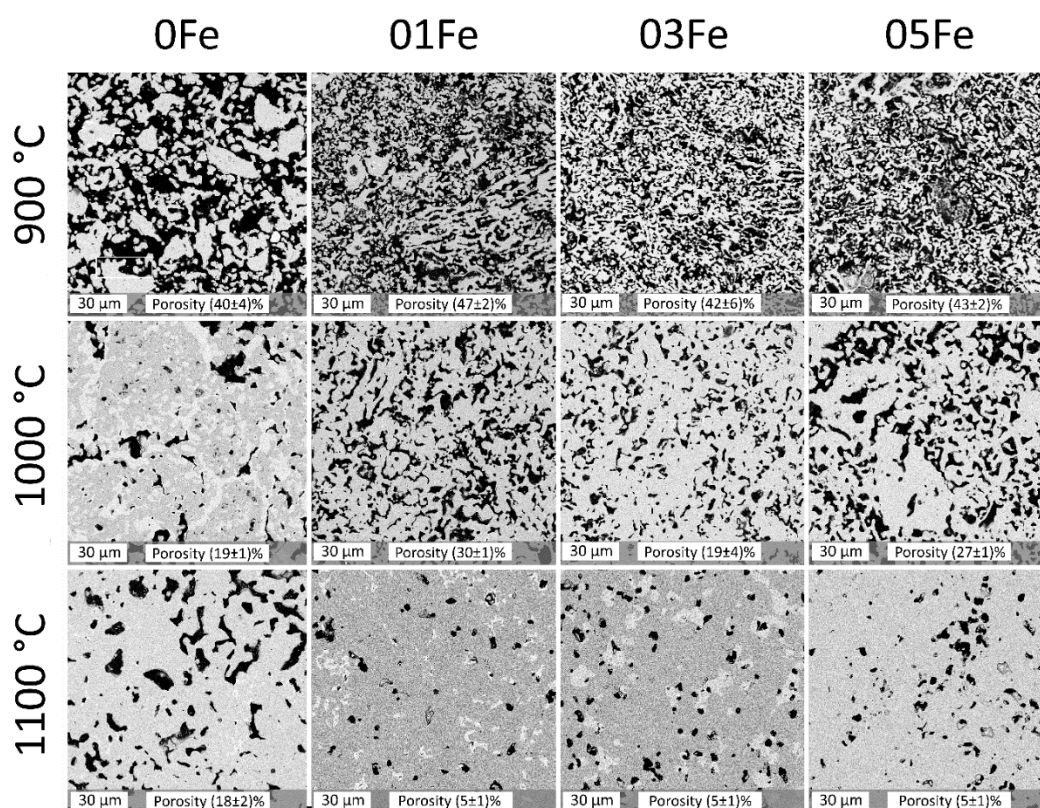
Temperature range	Thermal expansion coefficient TEC [ $\times 10^{-6} \text{ K}^{-1}$ ]		Activation energy for the electrical conductivity $E_A$ [eV]					
	50 °C- 600	600 °C- 900 °C	200 °C - 400 °C			450 °C- 650 °C		
$T_{\text{sintering}}/composition$	1100 °C		900 °C	1000 °C	1100 °C	900 °C	1000 °C	1100 °C
0Fe	9.57	13.01	0.57	0.47	0.37	0.22	0.22	0.25
01Fe	10.15	14.52	0.41	0.43	0.33	0.20	0.21	0.21
03Fe	10.58	18.57	0.53	0.58	0.31	0.21	0.22	0.25
05Fe	9.19	12.81	0.70	0.69	0.26	0.25	0.25	0.27

374

### 375 **3.3. Microstructural properties of sintered materials**

376 In order to characterise the properties of the materials in more detail, XRD and SEM/EDS  
377 analyses of the differently sintered pellets were performed. Images of polished cross-sections of all of  
378 the samples are presented in Figure 7, with accompanying elemental maps and chemical compositions  
379 in the supplementary materials (Figure S1, Table S1). Based on the images, the porosities of the pellets  
380 were determined and the values are included in the figure. The samples sintered at 900 °C showed  
381 similar, porous microstructures (porosities ~40–47%). For the samples containing iron, the particle  
382 sizes seemed to be smaller than for the non-substituted sample, where large well-sintered structures  
383 could be found. For samples sintered at 1000 °C the porosities were considerably lower (~20–30%),  
384 and a clear difference in the microstructure was obtained for the 0Fe sample. It was characterised by  
385 high density and showed the presence of different phases (different shades of grey). The iron-doped  
386 samples showed high density and a small amount of secondary phases. For the samples sintered at  
387 1100 °C, the microstructure was quite dense for all samples (porosities 5–20%), and the presence of  
388 secondary phases with different chemical compositions were detected for the 0Fe, 01Fe and 03Fe  
389 samples in increasing amounts, as can be expected from the XRD data. For the 05Fe sample, no  
390 inhomogeneity in the chemical composition was detected by SEM/EDS. XRD analyses of the pellet  
391 samples shown in Figure 7 were performed on powders obtained from crushed pellets (XRD spectra  
392 are presented in Figure S2). The structural results comply with other data. For a sintering temperature  
393 of 900 °C, the phase composition was relatively simple, and pure spinels were obtained (either in cubic,  
394 or cubic + tetragonal form) with a minor CuO phase for the 0Fe and 01Fe. Sintering at temperatures of  
395 1000 °C and above resulted in the formation of new phases. By analysing the phase diagrams, it can be  
396 seen that above 900 °C, the formation of a  $\text{CuMnO}_2$  phase started [20], with the formation of a  
397  $\text{Cu}_5\text{Mn}_4\text{O}_9$  phase above 975 °C [18]. Generally, based on the results and the published phase diagrams,  
398 the structure of the Mn-Cu spinels is retained up to <1000 °C.





399

400

**Figure 7.** SEM cross-section images of pellets sintered at different temperatures.

401

### 3.4. General discussion

402

Based on the obtained results, the effect of iron substitution in the Mn-Cu oxide spinel can be discussed. In general, Mn-Cu-based spinels are complex materials, which exhibit quite narrow single-phase regions in phase diagrams. By using a specific Mn:Cu ratio (e.g. 1.7:1.3), it is possible to obtain a pure cubic phase at room temperature, and up to ~600 °C, where CuO starts forming. By adding iron, the stability of the spinel lattice is extended. At room temperature, the 05Fe spinel is a mixture of cubic and tetragonal phases, that upon heating to >400 °C form a single cubic phase, which does not show decomposition into CuO upon further heating. Stabilisation of the spinel phase is important, as for the CuO-containing compositions, reduction to Cu<sub>2</sub>O happens at high temperatures. This reduction induces volume changes and can have a negative impact on the material's stability. Due to the precipitation of CuO, the electrical conductivities of the spinels differ. Precipitation of CuO results in lowering of the electrical conductivity, evidenced by a maxima in the conductivity curves, which indicates an important role of copper in the electrical conductivity. By adding Fe, CuO formation is suppressed, and the electrical conductivity follows a pattern expected for a thermally activated semiconductor with visible phase transition to a fully cubic structure.

416

### 417 **3.5. Possible application of the iron-substituted Mn-Cu spinel in solid oxide cells**

418 Though not specifically discussed above, iron-substituted spinels are being developed as potential  
419 protective coating materials for steel interconnects for high-temperature solid oxide cells. Currently,  
420 the state of the art is the  $\text{MnCo}_2\text{O}_4$  spinel, which shows good protective behaviour, but contains  
421 harmful and nonsustainably mined cobalt. Also, there is a strong need for cobalt in the rapidly  
422 developing Li-ion market. The results obtained in this work point to the potential applicability of the  
423 newly developed materials as protective coatings:

- 424 • Values of the TEC for the spinels might be considered to be compatible with Crofer 22 APU [55]  
425 or 441-type ferritic steel [56], which are used for the fabrication of SOFC interconnects;
- 426 • Electrical conductivity of the spinels is sufficiently high at operating temperatures ( $> 10 \text{ S cm}^{-1}$   
427 at 700–800 °C) [57];
- 428 • Iron substitution improves the sinterability of the spinels. Typically, the coatings are sintered  
429 via a reduction and subsequent reoxidation process. Lowering the sintering temperature can  
430 help with decreasing the reoxidation temperature from 900 °C [58] to 800°C or time used in  
431 coating densification process with the comparison of sintering condition for state of the art  
432  $\text{Mn}_2\text{CoO}_4$ .
- 433 • Iron-substituted spinels show thermochemical stability in oxidising conditions at high  
434 temperatures.

435 To prove the suitability of the materials for protective coatings for steel interconnects, further tests  
436 need to be carried out: specifically, issues including optimization of the coating process, sintering  
437 conditions, adhesion test, reactivity with Cr, area-specific resistant measurements and long-term  
438 corrosion properties (e.g. oxide scale growth kinetics) need to be evaluated. From a materials  
439 perspective, however, Fe-modified Mn-Cu spinels seem to have suitable physico-chemical properties  
440 for a successful protective coating.

441

## 442 **4. Conclusions**

443 In this work, Fe substituted  $\text{Mn}_{1.7}\text{Cu}_{1.3-x}\text{Fe}_x\text{O}_4$  spinel-based ceramics ( $x=0, 0.1, 0.3, 0.5$ ) were synthesised  
444 and characterised. Adding small amount of Fe ( $x = 0.1$ ) does not alter the properties considerably. On  
445 the other hand, adding more iron ( $x = 0.3$  or  $0.5$ ) results in the formation of the tetragonal spinel due  
446 to Jahn-Teller distortion of the octahedra, the change in electrical conductivity properties, and  
447 improved stability of the spinel phase (less or no CuO formation). The sinter-activity of the powders is

448 increased with the addition of iron, whereas the thermal expansion remains similar. Iron stabilised the  
449 spinel phase, thus no CuO is reduced at high temperatures, and thermal stability of the spinels is  
450 improved. The addition of iron results in lowered electrical conductivity. For the 0Fe and 01Fe a  
451 maxima in electrical conductivity values were found and correlated to the formation of the CuO phase.  
452 For the 03Fe and 05Fe, no maxima were found, and the samples follow a linear, thermally activated  
453 behaviour.

454 To conclude, the results show that partial substitution of Cu by Fe in the Mn-Cu spinel leads to  
455 suppression of the formation of CuO<sub>x</sub> at high temperatures, which improves the thermomechanical  
456 properties and sinterability of the ceramics. The concomitant trade-off in electrical properties leaves  
457 absolute values of conductivity on the level desirable for SOFC/SOEC applications.

## 458 **Acknowledgments**

459 This project is supported by National Science Centre (NCN) Harmonia 9 project number UMO-  
460 2017/26/M/ST8/00438: “Quest for novel materials for solid oxide cell interconnect coatings”. Funding  
461 of WETI PG is also gratefully acknowledged.

## 462 References

- 463 [1] Q. Zhao, Z. Yan, C. Chen, J. Chen, Spinel: Controlled Preparation, Oxygen  
464 Reduction/Evolution Reaction Application, and Beyond, *Chem. Rev.* (2017)  
465 *acs.chemrev.7b00051*. <https://doi.org/10.1021/acs.chemrev.7b00051>.
- 466 [2] K.M. Shaju, P.G. Bruce, Nano-LiNi<sub>0.5</sub>Mn<sub>1.5</sub>O<sub>4</sub> spinel: a high power electrode for Li-ion  
467 batteries, *Dalt. Trans.* 0 (2008) 5471. <https://doi.org/10.1039/b806662k>.
- 468 [3] Y. Zhu, X. Ji, Z. Wu, W. Song, H. Hou, Z. Wu, X. He, Q. Chen, C.E. Banks, Spinel NiCo<sub>2</sub>O<sub>4</sub>  
469 for use as a high-performance supercapacitor electrode material: Understanding of its  
470 electrochemical properties, *J. Power Sources.* 267 (2014) 888–900.  
471 <https://doi.org/10.1016/J.JPOWSOUR.2014.05.134>.
- 472 [4] S. Chen, X. Zhou, W. Song, J. Sun, H. Zhang, J. Jiang, L. Deng, S. Dong, X. Cao, Mg<sub>2</sub>SiO<sub>4</sub>  
473 as a novel thermal barrier coating material for gas turbine applications, *J. Eur. Ceram. Soc.* 39  
474 (2019) 2397–2408. <https://doi.org/10.1016/j.jeurceramsoc.2019.02.016>.
- 475 [5] M. Zawadzki, W. Walerczyk, F.E. López-Suárez, M.J. Illán-Gómez, A. Bueno-López,  
476 CoAl<sub>2</sub>O<sub>4</sub> spinel catalyst for soot combustion with NO<sub>x</sub>/O<sub>2</sub>, *Catal. Commun.* 12 (2011) 1238–  
477 1241. <https://doi.org/10.1016/J.CATCOM.2011.04.021>.
- 478 [6] S. Takahashi, H. Ogawa, A. Kan, Electronic states and cation distributions of MgAl<sub>2</sub>O<sub>4</sub> and  
479 Mg<sub>0.4</sub>Al<sub>1.6</sub>O<sub>4</sub> microwave dielectric ceramics, *J. Eur. Ceram. Soc.* 38 (2018) 593–598.  
480 <https://doi.org/10.1016/j.jeurceramsoc.2017.08.022>.
- 481 [7] H. Jia, W. Zhou, H. Nan, J. Dong, Y. Qing, F. Luo, D. Zhu, Enhanced high temperature  
482 dielectric polarization of barium titanate/magnesium aluminum spinel composites and their  
483 potential in microwave absorption, *J. Eur. Ceram. Soc.* 40 (2020) 728–734.  
484 <https://doi.org/10.1016/j.jeurceramsoc.2019.11.003>.
- 485 [8] Y. Liu, J.W. Fergus, K. Wang, C. Dela Cruz, Crystal Structure, Chemical Stabilities and  
486 Electrical Conductivity of Fe-Doped Manganese Cobalt Spinel Oxides for SOFC Interconnect  
487 Coatings, *J. Electrochem. Soc.* (2013). <https://doi.org/10.1149/2.114311jes>.
- 488 [9] Y. Zhou, S. Sun, J. Song, S. Xi, B. Chen, Y. Du, A.C. Fisher, F. Cheng, X. Wang, H. Zhang,  
489 Z.J. Xu, Enlarged Co–O Covalency in Octahedral Sites Leading to Highly Efficient Spinel  
490 Oxides for Oxygen Evolution Reaction, *Adv. Mater.* 30 (2018) 1–7.  
491 <https://doi.org/10.1002/adma.201802912>.
- 492 [10] R. Metz, J.P. Caffin, R. Legros, A. Rousset, The preparation, characterization and electrical

- 493 properties of copper manganite spinels,  $Cu_xMn_{3-x}O_4$ ,  $0 \leq x \leq 1$ , *J. Mater. Sci.* 24 (1989) 83–  
494 87. <https://doi.org/10.1007/BF00660936>.
- 495 [11] G.T. Bhandage, H. V Keer, Structural and magnetic properties of the  $Cu_xCd_{1-x}Mn_2O_4$   
496 system, *J. Phys. C Solid State Phys.* 8 (1975) 501–506.
- 497 [12] G.T. Bhandage, H. V Keer, A correlation of the physical properties of the  $Ni_xCu_{1-x}Mn_2O_4$   
498 system, *J. Phys. C Solid State Phys.* 9 (1976) 1325–1331.
- 499 [13] R. Buhl, Manganites spinelles purs d'elements de transition preparations et structures  
500 cristallographiques, *J. Phys. Chem. Solids.* 30 (1969) 805–812. [https://doi.org/10.1016/0022-3697\(69\)90275-3](https://doi.org/10.1016/0022-3697(69)90275-3).  
501
- 502 [14] T. Fukunaga, N. Ryumon, N. Ichikuni, S. Shimazu, Characterization of CuMn-spinel catalyst  
503 for methanol steam reforming, *Catal. Commun.* 10 (2009) 1800–1803.  
504 <https://doi.org/10.1016/j.catcom.2009.06.001>.
- 505 [15] P. Ma, Q. Geng, X. Gao, T. Zhou, S. Yang, G. Liu, Aqueous solution-derived  $CuMn_2O_4$   
506 ceramic films for spectrally selective solar absorbers, *Ceram. Int.* (2016).  
507 <https://doi.org/10.1016/j.ceramint.2016.09.062>.
- 508 [16] J. Li, C. Xiong, J. Li, D. Yan, J. Pu, B. Chi, L. Jian, Investigation of  $MnCu_0.5Co_1.5O_4$  spinel  
509 coated SUS430 interconnect alloy for preventing chromium vaporization in intermediate  
510 temperature solid oxide fuel cell, *Int. J. Hydrogen Energy.* 42 (2017).  
511 <https://doi.org/10.1016/j.ijhydene.2017.05.074>.
- 512 [17] F.C.M. Driessens, G.D. Rieck, Phase Equilibria in the System Cu-Mn-O, *J. Inorg. Gen. Chem.*  
513 351 (1967) 48–62. <https://doi.org/10.1002/zaac.19673510108>.
- 514 [18] P. Wei, M. Bieringer, L.M.D. Cranswick, A. Petric, In situ high-temperature X-ray and neutron  
515 diffraction of Cu-Mn oxide phases, *J. Mater. Sci.* 45 (2010) 1056–1064.  
516 <https://doi.org/10.1007/s10853-009-4042-2>.
- 517 [19] C. Maunders, B.E. Martin, P. Wei, A. Petric, G.A. Botton, Investigation of the electronic  
518 structure of the cubic spinel  $Cu_{1.2}Mn_{1.8}O_4$  using electron energy loss spectroscopy, *Solid  
519 State Ionics.* 179 (2008) 718–724. <https://doi.org/10.1016/j.ssi.2008.04.029>.
- 520 [20] B.E. Martin, A. Petric, Electrical properties of copper-manganese spinel solutions and their  
521 cation valence and cation distribution, *J. Phys. Chem. Solids.* (2007).  
522 <https://doi.org/10.1016/j.jpcs.2007.06.019>.
- 523 [21] P. Wei, Spinel coatings for Solid Oxide Fuel Cell interconnects and crystal structure of Cu-Mn-



- 524 O, McMaster University, Canada, 2009.
- 525 [22] A. Petric, H. Ling, Electrical conductivity and thermal expansion of spinels at elevated  
526 temperatures, *J. Am. Ceram. Soc.* (2007). <https://doi.org/10.1111/j.1551-2916.2007.01522.x>.
- 527 [23] Z. Sun, R. Wang, A.Y. Nikiforov, S. Gopalan, U.B. Pal, S.N. Basu, CuMn<sub>1.8</sub>O<sub>4</sub> protective  
528 coatings on metallic interconnects for prevention of Cr-poisoning in solid oxide fuel cells, *J.*  
529 *Power Sources*. 378 (2018) 125–133. <https://doi.org/10.1016/j.jpowsour.2017.12.031>.
- 530 [24] Z. Sun, S. Gopalan, U.B. Pal, S.N. Basu, Cu<sub>1.3</sub>Mn<sub>1.7</sub>O<sub>4</sub> spinel coatings deposited by  
531 electrophoretic deposition on Crofer 22 APU substrates for solid oxide fuel cell applications,  
532 *Surf. Coatings Technol.* 323 (2017) 49–57. <https://doi.org/10.1016/j.surfcoat.2016.09.028>.
- 533 [25] W. Huang, S. Gopalan, U.B. Pal, S.N. Basu, Evaluation of Electrophoretically Deposited  
534 CuMn<sub>[sub 1.8]O[sub 4]</sub> Spinel Coatings on Crofer 22 APU for Solid Oxide Fuel Cell  
535 Interconnects, *J. Electrochem. Soc.* (2008). <https://doi.org/10.1149/1.2975367>.
- 536 [26] P. Zielke, A.C. Wulff, X. Sun, S.H. Jensen, R. Kiebach, H.L. Frandsen, P. Norby, A. Hagen,  
537 Investigation of a Spinel-forming Cu-Mn Foam as an Oxygen Electrode Contact Material in a  
538 Solid Oxide Cell Single Repeating Unit, *Fuel Cells*. 17 (2017) 730–734.  
539 <https://doi.org/10.1002/face.201700005>.
- 540 [27] B. Talic, P.V. Hendriksen, K. Wiik, H.L. Lein, Thermal expansion and electrical conductivity  
541 of Fe and Cu doped MnCo<sub>2</sub>O<sub>4</sub> spinel, *Solid State Ionics*. 326 (2018) 90–99.  
542 <https://doi.org/10.1016/j.ssi.2018.09.018>.
- 543 [28] D. Szymczewska, S. Molin, P. Hendriksen, P. Jasiński, Microstructure and Electrical Properties  
544 of Fe,Cu Substituted (Co,Mn)<sub>3</sub>O<sub>4</sub> Thin Films, *Crystals*. 7 (2017) 185.  
545 <https://doi.org/10.3390/cryst7070185>.
- 546 [29] T. Brylewski, A. Kruk, M. Bobruk, A. Adamczyk, J. Partyka, P. Rutkowski, Structure and  
547 electrical properties of Cu-doped Mn-Co-O spinel prepared via soft chemistry and its  
548 application in intermediate-temperature solid oxide fuel cell interconnects, *J. Power Sources*.  
549 333 (2016) 145–155. <https://doi.org/10.1016/j.jpowsour.2016.09.136>.
- 550 [30] B. Talic, P.V. Hendriksen, K. Wiik, H.L. Lein, Thermal expansion and electrical conductivity  
551 of Fe and Cu doped MnCo<sub>2</sub>O<sub>4</sub> spinel, *Solid State Ionics*. (2018).  
552 <https://doi.org/10.1016/j.ssi.2018.09.018>.
- 553 [31] S. Molin, P. Jasinski, L. Mikkelsen, W. Zhang, M. Chen, P. V. Hendriksen, Low temperature  
554 processed MnCo<sub>2</sub>O<sub>4</sub> and MnCo<sub>1.8</sub>Fe<sub>0.2</sub>O<sub>4</sub> as effective protective coatings for solid oxide fuel

- 555 cell interconnects at 750 °C, *J. Power Sources*. 336 (2016) 408–418.  
556 <https://doi.org/10.1016/j.jpowsour.2016.11.011>.
- 557 [32] E. Zanchi, B. Talic, A.G. Sabato, S. Molin, A.R. Boccaccini, F. Smeacetto, Electrophoretic co-  
558 deposition of Fe<sub>2</sub>O<sub>3</sub> and Mn<sub>1.5</sub>Co<sub>1.5</sub>O<sub>4</sub>: Processing and oxidation performance of Fe-doped  
559 Mn-Co coatings for solid oxide cell interconnects, *J. Eur. Ceram. Soc.* 39 (2019).  
560 <https://doi.org/10.1016/j.jeurceramsoc.2019.05.024>.
- 561 [33] S. Molin, A.G. Sabato, H. Javed, G. Cempura, A.R. Boccaccini, F. Smeacetto, Co-deposition  
562 of CuO and Mn<sub>1.5</sub>Co<sub>1.5</sub>O<sub>4</sub> powders on Crofer22APU by electrophoretic method :  
563 Structural , compositional modifications and corrosion properties, *Mater. Lett.* 218 (2018) 329–  
564 333. <https://doi.org/10.1016/j.matlet.2018.02.037>.
- 565 [34] N. Grünwald, Y.J. Sohn, X. Yin, N.H. Menzler, O. Guillon, R. Vaßen, Microstructure and  
566 phase evolution of atmospheric plasma sprayed Mn-Co-Fe oxide protection layers for solid  
567 oxide fuel cells, *J. Eur. Ceram. Soc.* 39 (2019) 449–460.  
568 <https://doi.org/10.1016/j.jeurceramsoc.2018.08.027>.
- 569 [35] S. Joshi, A. Petric, Nickel substituted CuMn<sub>2</sub>O<sub>4</sub> spinel coatings for solid oxide fuel cell  
570 interconnects, *Int. J. Hydrogen Energy*. 42 (2017) 5584–5589.  
571 <https://doi.org/10.1016/j.ijhydene.2016.08.075>.
- 572 [36] M. Salavati-Niasari, F. Davar, M. Farhadi, Synthesis and characterization of spinel-type  
573 CuAl<sub>2</sub>O<sub>4</sub> nanocrystalline by modified sol-gel method, *J. Sol-Gel Sci. Technol.* (2009).  
574 <https://doi.org/10.1007/s10971-009-1940-3>.
- 575 [37] J. Lin, Y. He, X. Du, Q. Lin, H. Yang, H. Shen, Structural and Magnetic Studies of Cr<sup>3+</sup>  
576 Substituted Nickel Ferrite Nanomaterials Prepared by Sol-Gel Auto-Combustion, *Crystals*. 8  
577 (2018) 384. <https://doi.org/10.3390/cryst8100384>.
- 578 [38] M. Bobruk, K. Durczak, J. Dąbek, T. Brylewski, Structure and Electrical Properties of Mn-Cu-  
579 O Spinel, *J. Mater. Eng. Perform.* 26 (2017) 1598–1604. <https://doi.org/10.1007/s11665-017-2588-8>.
- 581 [39] Z. Sun, S. Gopalan, U.B. Pal, S.N. Basu, Cu<sub>1.3</sub>Mn<sub>1.7</sub>O<sub>4</sub> spinel coatings deposited by  
582 electrophoretic deposition on Crofer 22 APU substrates for solid oxide fuel cell applications,  
583 *Surf. Coatings Technol.* (2017). <https://doi.org/10.1016/j.surfcoat.2016.09.028>.
- 584 [40] M. Bobruk, K. Brylewska, K. Durczak, K. Wojciechowski, A. Adamczyk, T. Brylewski,  
585 Synthesis of manganese-cobalt spinel via wet chemistry methods and its properties, *Ceram. Int.*  
586 43 (2017) 15597–15609. <https://doi.org/10.1016/j.ceramint.2017.08.116>.

- 587 [41] W. -S Hong, L.C. De Jonghe, X. Yang, M.N. Rahaman, Reaction Sintering of ZnO-Al<sub>2</sub>O<sub>3</sub>, J.  
588 Am. Ceram. Soc. (1995). <https://doi.org/10.1111/j.1151-2916.1995.tb07957.x>.
- 589 [42] J. Marín-Romero, L. Fuentes-Cobas, J. Rodríguez-Carvajal, C. Tabasco-Novelo, P. Quintana,  
590 Structure of a Novel Spinel Li<sub>0.5</sub>Zn<sub>5/3</sub>Sb<sub>2.5/3</sub>O<sub>4</sub> by Neutron and Synchrotron Diffraction  
591 Analysis, Crystals. 7 (2017) 280. <https://doi.org/10.3390/cryst7090280>.
- 592 [43] A.E. Danks, S.R. Hall, Z. Schnepf, The evolution of “sol-gel” chemistry as a technique for  
593 materials synthesis, Mater. Horizons. (2016). <https://doi.org/10.1039/c5mh00260e>.
- 594 [44] M. Galceran, · M C Pujol, · M Aguiló, · F Díaz, M. Aguiló, F. Díaz, Sol-gel modified Pechini  
595 method for obtaining nanocrystalline KRE(WO<sub>4</sub>)<sub>2</sub> (RE = Gd and Yb) Sol-gel modified Pechini  
596 method for obtaining nanocrystalline KRE(WO<sub>4</sub>)<sub>2</sub> (RE = Gd and Yb), Artic. J. Sol-Gel Sci.  
597 Technol. 42 (2007) 79–88. <https://doi.org/10.1007/s10971-006-1517-3>.
- 598 [45] C.W. Bale, E. Bélisle, P. Chartrand, S.A. Deckerov, G. Eriksson, A.E. Gheribi, K. Hack, I.H.  
599 Jung, Y.B. Kang, J. Melançon, A.D. Pelton, S. Petersen, C. Robelin, J. Sangster, P. Spencer,  
600 M.A. Van Ende, FactSage thermochemical software and databases, 2010-2016, Calphad  
601 Comput. Coupling Phase Diagrams Thermochem. 54 (2016) 35–53.  
602 <https://doi.org/10.1016/j.calphad.2016.05.002>.
- 603 [46] L.J. van der Pauw, A method of measuring the resistivity and Hall coefficient on samples of  
604 arbitrary shape, Philips Res. Reports. (1958).  
605 <https://doi.org/537.723.1:53.081.7+538.632:083.9>.
- 606 [47] R. Landauer, Electrical conductivity in inhomogeneous media, in: AIP Conf. Proc., AIP  
607 Publishing, 2008: pp. 2–45. <https://doi.org/10.1063/1.311150>.
- 608 [48] A. Purwanto, A. Fajar, H. Mugirahardjo, J.W. Fergus, K. Wang, Cation distribution in spinel  
609 (Mn,Co,Cr)O<sub>4</sub> at room temperature, J. Appl. Crystallogr. 43 (2010) 394–400.  
610 <https://doi.org/10.1107/S0021889810008150>.
- 611 [49] H.A. Jahn, E. Teller, Stability of polyatomic molecules in degenerate electronic states - I—  
612 Orbital degeneracy, Proc. R. Soc. 161 (1937) 220–235.
- 613 [50] J.D. Dunitz, L.E. Orgel, Electronic properties of transition-metal oxides—I. Distortions from  
614 cubic symmetry, J. Phys. Chem. Solids. 3 (1957) 20–29. [https://doi.org/10.1016/0022-3697\(57\)90043-4](https://doi.org/10.1016/0022-3697(57)90043-4).
- 615  
616 [51] N. Baffier, M. Huber, Etude par diffraction des rayons X et des neutrons, des relations entre  
617 distribution cationique et distorsion cristalline dans les ferro-manganites spinelles: xMnO<sub>3</sub> +



- 618 (1 - x) Cu(Fe,Cr)2O4, *J. Phys. Chem. Solids.* 33 (1972) 737–747. [https://doi.org/10.1016/0022-](https://doi.org/10.1016/0022-3697(72)90081-9)  
619 3697(72)90081-9.
- 620 [52] Y. Zhu, K. Mimura, M. Isshiki, Oxidation mechanism of Cu2O to CuO at 600-1050 °C, *Oxid.*  
621 *Met.* 62 (2004) 207–222. <https://doi.org/10.1007/s11085-004-7808-6>.
- 622 [53] T. Narushima, H. Tsukamoto, T. Yonezawa, High temperature oxidation event of gelatin  
623 nanoskin-coated copper fine particles observed by in situ TEM, *AIP Adv.* 2 (2012).  
624 <https://doi.org/10.1063/1.4759498>.
- 625 [54] N. Ponpandian, P. Balaya, A. Narayanasamy, Electrical conductivity and dielectric behaviour  
626 of nanocrystalline NiFe<sub>2</sub>O<sub>4</sub> spinel, *J. Phys. Condens. Matter.* 14 (2002) 3221–3237.  
627 <https://doi.org/10.1088/0953-8984/14/12/311>.
- 628 [55] M. Stygar, K. Matsuda, S. Lee, T. Brylewski, Corrosion Behavior of Crofer 22APU for  
629 Metallic Interconnects in Single and Dual Atmosphere Exposures at 1073 K, 131 (2017).  
630 <https://doi.org/10.12693/APhysPolA.131.1394>.
- 631 [56] Stainless Steel Type 441 – Rolled Metal Products | Stainless, Aluminum & Specialty Alloys,  
632 (n.d.). <https://rolledmetalproducts.com/stainless-steel-type-441/> (accessed March 9, 2020).
- 633 [57] C. Goebel, A.G. Fefekos, J.E. Svensson, J. Froitzheim, Does the conductivity of interconnect  
634 coatings matter for solid oxide fuel cell applications?, *J. Power Sources.* 383 (2018) 110–114.  
635 <https://doi.org/10.1016/j.jpowsour.2018.02.060>.
- 636 [58] M. Bobruk, S. Molin, M. Chen, T. Brylewski, P. V. Hendriksen, Sintering of  
637 MnCo2O4 coatings prepared by electrophoretic deposition, *Mater. Lett.* (2018).  
638 <https://doi.org/10.1016/j.matlet.2017.12.046>.
- 639